Int J Adv Manuf Technol (2016) 82:197–209
DOI 10.1007/s00170-015-7367-9

ORIGINAL ARTICLE

Replication of microstructured tools for electrochemical machining applications

Konstantin Weißhaar[1] · **Martin Weinmann**[1] · **Anne Jung**[2] · **Olivier Weber**[3] · **Harald Natter**[1]

Received: 25 February 2015 / Accepted: 21 May 2015 / Published online: 9 June 2015

Abstract Electrochemical machining (ECM) is a powerful method to machine metals independently of their mechanical properties. Micro-sized structures can be formed with high precision. For this purpose, it is necessary to manufacture tools with adequately fine structures. Conventional ECM tools were manufactured by micro-drilling, -milling, -turning, etc. Depending on the complexity of the structures, these techniques are very elaborate and expensive. Recently, a new procedure, which combines photolithography and electroforming, the so-called PhoGaTool process (photolithographic electroforming of ECM tools), was published. In the present work, we demonstrate how this method can also be used for copying ECM tools that were conventionally manufactured. A copy of an industrial PECM tool (precise electrochemical machining) was manufactured and used for the structural characterization and determination of the replication accuracy. The electroforming parameters like deposition conditions, bath composition as well as physical and chemical parameters were optimized for model systems. The inclusion of bath additives in the metal matrix during the deposition leads to micro-stresses, hence in this contribution, an alternative additive-free electrolyte was used. The accuracy of the process was investigated by means of confocal laser scanning microscopy. Average deviations of the structure depth and the lateral structure dimensions are in the range of 5 %.

Keywords Electrochemical micromachining · Tool replication · Tool manufacturing · Tool precision · Electroforming

✉ Harald Natter
h.natter@mx.uni-saarland.de

[1] Physical Chemistry, Saarland University, Campus B2 2, 66123 Saarbrücken, Germany

[2] Department of Applied Mechanics, Saarland University, Saarbrücken, Germany

[3] Institute of Production Engineering, Saarland University, Saarbrücken, Germany

1 Introduction

The tendency to manufacture very small structures with dimensions below 500 μm requires techniques and tools with the appropriate precision. A suitable method is the electrochemical machining (ECM) process [1, 2], which was invented in the late 1929 by W. Gusseff. The metallic workpiece is structured by selective anodic dissolution in a conductive electrolyte (e.g., sodium nitrate), which is pumped through the gap between cathode and anode at a high speed. The machining with this process is independent of the material's mechanical properties; the only requirement is the electrical conductivity of the chosen material. The applied voltage causes a current flow between the positive polarized anode (workpiece) and the negative polarized cathode (tool). This leads to a controlled and localized dissolution of the anode. The shape of the final workpiece results from the corresponding tool geometry. For example, if the workpiece should have a simple cylindrical shape, the ECM tool consists of a metal sheet with a hole in it which has a diameter slightly larger than the final cylindrical structure. Relief-like structures were transferred negatively on the workpiece (Fig. 1).

The advantages of the ECM process are as follows:

- formation of complex structures with a high surface quality in only one production step [3, 4],
- almost no tool wear [5] due to the applied voltage,

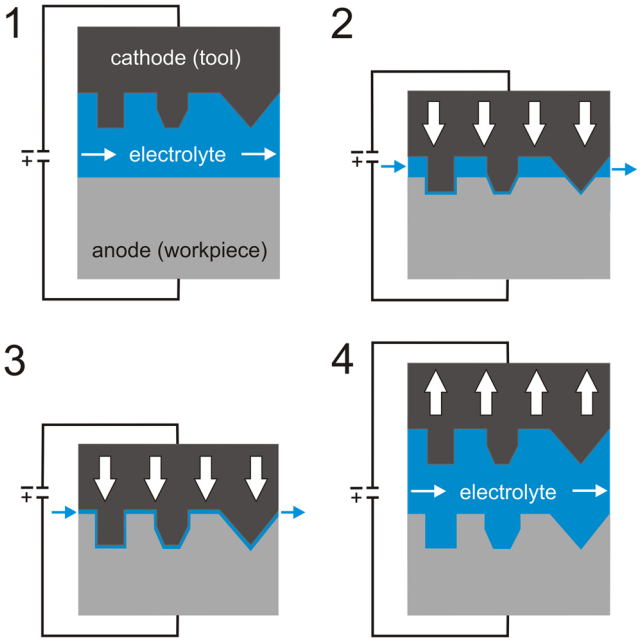

Fig. 1 Schematic view of the ECM process

- no internal stress induced by the process [6],
- cost-efficiency [7].

A recent development of ECM is the precise electrochemical machining (PECM) [6] and the pulse electrochemical micromachining (PEMM) [8, 9]. In contrast to the classical ECM process, the applied voltage is pulsed and additionally the tool is vibrating. If the tool reaches the lower reversal point of the cycle, the voltage pulse takes place and the tool moves back to the starting position (upper reversal point). In this state, the electrolyte removes all gaseous and solid removal products from the surface of the workpiece. In this way, the PECM technique allows much smaller interelectrode gaps (several micrometers) than the conventional ECM process because there is no possibility for a plugging of the work gap by the as-mentioned removal products. In the case of a large gap size, the scattering of the electronic field lines leads to an undesired dissolution of the boundary areas which leads to an imprecise workpiece structure. Obviously, the precision of the workpiece will be increased by a reduced gap size. A detailed comparison of ECM and PEMM is given by Bhattacharyya et al. [10].

The production of micro-sized structures by micro-ECM [11, 12] requires corresponding micro-sized tools [13]. Nowadays, most micro-sized tools are fabricated using conventional methods like micro-drilling, -milling [14], or -turning [15]. Disadvantages of these methods [16] are high mechanical and thermal loads on the manufactured tool. Another non-conventional method is laser beam machining [10, 17]. These techniques require special tools and machines and therefore the manufacturing of micro-ECM tools is elaborate and expensive. A new process chain, called PhoGaTool, described by Weinmann et al. [18], enables the production of microstructured tools with comparably less effort. This method consists of several steps including structuring by photolithography, casting with silicone and resin, and finally electroforming. Thus, low-cost productions of microstructured ECM tools with a high precision are possible. In order to copy existing surfaces, a modification of the PhoGaTool process is predestinated. As the microstructure is already manufactured using conventional methods (e.g., mechanical machining, 3D printing), the photolithographic steps can be avoided. The micro-ECM tool can be manufactured in a four-step procedure. In a first step, the microstructure is molded with silicone. The silicone model is used for the preparation of a bath model, which is covered with a conductive layer (nickel or gold). Finally, the tool is electroformed in a nickel electrolyte. The aim of this work is the formation of structures with dimensions below 500 μm. For this reason, the microstructure of the electroformed material has to be nanocrystalline because a coarse-grained structure decreases the mechanical stability and also the replication accuracy. The formation of nanostructures in an electroforming process can be achieved by properly selecting the plating conditions that influence the electrocrystallization [19, 20].

Benefits of this copying process are as follows:

- The mechanically manufactured master tool is not abraded because it is only used for the replication process.
- This procedure enables the production of several tools in parallel, which can be used for parallel series production or for very wear-intensive production processes.
- The use of a micro-ECM tool copy is cheaper than conventional production.
- The components (chemicals, electronic devices) are commercially available and very cost-effective.
- A wide range of materials can be used for the copy process of microstructures without undercuts.
- Due to a comparably simple manufacturing process and equipment, the process performance does not require highly trained experts.
- The equipment of the replication process is portable and can be used at every desired location.

In the present work, the accuracy of the described method is investigated. The copied electrode and the workpiece are analyzed by evaluating three-dimensional LSM micrographs. Furthermore, the electrolyte composition for the electroforming process is optimized by testing different additives and their influences on the resulting deposit properties.

2 Electrochemical nanostructuring of metals

Electrocrystallization describes the build-up of metal layers from the ionic state. It includes three sub-steps: mass transport in the electrolyte, cross-over of the interphase, and incorporation of the adatoms in the metal lattice. Interventions in at least one of these three sub-steps cause changes in the microstructure of the deposited metal. Inhibition describes the slowdown of the velocity of the sub-steps during electrocrystallization by addition of organic or inorganic substances. The most common inhibition mechanism to form nanomaterials is surface inhibition [21]. It describes the sorptive covering of the electrode surface. The production of nanomaterials requires the formation of new crystallites over the whole deposition time. From a thermodynamic point of view, the necessary amount of energy must be provided by the crystallization overpotential η_k. The crystallite formation velocity v shows the following dependence from the overall overpotential $|\eta|$ of the system [22–24]:

$$v = k_1 \exp\left(-\frac{k_2}{|\eta|}\right) \quad (1)$$

(k_1 is a constant of proportionality and k_2 a system specific constant)

An increase in the total overpotential causes an increasing crystallite formation velocity leading to the formation of many new crystallites and hence to the buildup of a fine-grained or nanocrystalline microstructure.

Without efficient surface inhibitors, the crystallites grow at low overpotentials prohibiting the formation of new crystallites due to accumulation of adatoms at the growth axis. With increasing coverage of the electrode surface by inhibitor molecules, the overpotential increases and therefore the overpotential for the formation of crystallites is exceeded. A large coverage of the electrode surface causes a reduced surface diffusion of the adatoms. An inhibition only occurs if the reduction of the metal ions and not the sorption of the inhibitors is the speed-limiting step.

Primary inhibitors are substances acting without changes in their chemical composition in the sub-steps of the electrocrystallization process. Secondary inhibitors only arise during the deposition by reduction, oxidation, or changes of the pH in the diffusion layer. Metal hydroxides, produced by hydrolysis in the diffusion layer, are of high importance as secondary inhibitors.

Nickel deposition is mostly affected by secondary inhibition. Amblard has shown that inhibition plays a significant role in the evolution of the microstructure of nickel deposits [25–28]. According to Amblard, the inhibition is caused by molecules selectively acting on distinct growth directions. The molecules are formed by the co-deposition of hydrogen at the cathode. Due to the high surface energy of nickel, nearly each molecule in the vicinity of the electrolyte/cathode interface will be adsorbed on the cathode surface. Possible adsorbates are H^+, OH^-, adsorbed metal ions, anions, or additives. Hence, even in additive-free electrolytes, there are inhibition effects caused by a variation in the pH, the potential, or the current leading to the formation of distinct microstructures. The strongest influence on the crystallite size and the microstructure is caused by organic additives. Potential benefits of additives are good brightness, grain refinement, reduction of uncontrolled deposit growth at edges, leveling, the prevention of pores, the reduction of internal stresses, and changes in the physical and mechanical properties. Additives act by adsorption on surfaces with high surface energy. The exact function and mechanism is up to now not well understood. In Sections 3 and 4, the influence of different plating parameters (additive type and amount, current density) on the microstructure of nickel deposits are described.

3 Experimental

3.1 Electroforming of nickel

3.1.1 Plating parameters and additives

For the electroforming process, a commercial nickel sulfamate electrolyte (Enthone GmbH, Langenfeld, Germany) was used at a temperature of 40 °C and a pH of 3.8. The depositions were performed using direct current plating at a current density of 20 mA cm^{-2}. The effect of 2-butyne-1,4-diol, the sodium salt of saccharine and naphthalene-1,3,6-trisulfonic acid trisodium salt (NTA) on the microstructure, crystallite size, and hardness were investigated. The additive concentrations are summarized in Table 1.

3.1.2 Chemical characterization of the deposits

Most organic additives and also their decomposition products can be determined by high-performance liquid chromatography (HPLC). According to the IC application note No. U-25 from Metrohm Ltd., reversed-phase chromatography (RP-HPLC) with UV detection and a prontosil 120-5-C18AQ 125×4.6 mm column was used for determining the concentration of saccharine and its decomposition products. The eluent for the analysis was prepared in the following way:

1. 2.722 g potassium dihydrogen phosphate monohydrate was dissolved in 1000 mL MilliQ water
2. The pH value was adjusted to 3 by adding H_3PO_4
3. 700 g of this solution was mixed with 237 g methanol
4. The solution was degassed with inert gas.

Table 1 Concentrations of the used additives

Saccharine		NTA		Butynediol	
g L^{-1}	mmol L^{-1}	g L^{-1}	mmol L^{-1}	g L^{-1}	mmol L^{-1}
0.10	0.49	0.18	0.41	0.02	0.23
0.40	1.94	0.72	1.66	0.06	0.69
0.70	3.40	1.26	2.90	1.00	11.62
1.00	4.85	1.80	4.14	1.40	16.28

Table 2 Process parameters for manufacturing of the master tool

	Roughing	Finishing	Polishing
Voltage (V)	9.5	7	14
Pulse frequency (Hz)	70	50	20
Pulse-on time (ms)	3.2	1.5	1
Tool feed rate (mm min^{-1})	0.3	0.06	0.110
Peak current (A)	300	200	650
Gap size (μm)	40	20	25

For NTA analysis, a column made of EU material 5 μm 150×4.0 mm was used. For preparation of the eluent, 5 mmol tetrabutylammonium hydrogen sulfate was adjusted to pH 3 with a mixture of NH_3/MeOH (60:40) and filled up to a volume of 1000 mL with MilliQ water. The content of NTA, saccharine, and their decomposition products in the electrolyte were analyzed by taking a sample (up to twice a day) from the plating bath. All samples were diluted with MilliQ water in a ratio of 1:100. Twenty microliters of the calibration standard and also 20 μL of the sample were injected onto the column (eluent flow 1 mL min^{-1}, temperature 20 °C).

3.2 Manufacturing of the master tool

A mechanically manufactured ECM tool was used to produce a workpiece, which consists of an Inconel 718 disc. The diameter of the workpiece is 18 mm and its thickness 3 mm. A photography of it is shown in Fig. 2 (left). The surface is structured with different geometries: flat sections (1), curved areas (2), sharp edges (3), honeycombed structures (4), holes (5), and structures with different depths (3, 4).

The workpiece was manufactured with an industrial production plant (PEMCenter800; PEMTec SNC, Forbach, France) in PECM mode. As electrolyte, a solution of 8 wt% $NaNO_3$ with a conductivity of 65 mS cm^{-1} (pH 7) was used. The electrolyte flow through the interelectrode gap (Table 2) was 2 L min^{-1} (pressure 4 bar) and the temperature was kept constant at 21 °C. The process parameters are summarized in Table 2.

3.3 Description of the replication process

The replication process consists of four steps (Fig. 3):

1. A silicone mold was made from the master tool (step 3)
2. The structure of the silicone mold was casted with resin (step 4)
3. After curing, the bath model was covered with a conductive layer (step 5)
4. The final step is the electroforming of the ECM tool (step 6).

3.3.1 Preparation of the silicone cast

For the preparation of the silicone cast (Fig. 3, step 3), the master tool was cleaned with acetone and dried at room temperature. Afterwards, it was placed in a casting box with the structured side facing upwards. The two components of the silicone (Elastosil RT 601; Wacker Chemie AG, Munich, Germany) were mixed together and subsequently degassed in vacuum. The casting box was filled with the silicone mixture

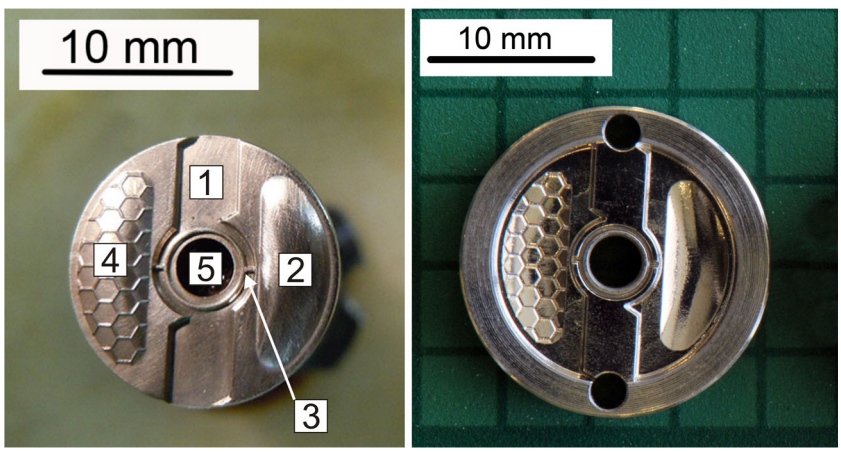

Fig. 2 Original ECM tool (*left-hand side*) and workpiece with test structures used for the replication process (*right-hand side*)

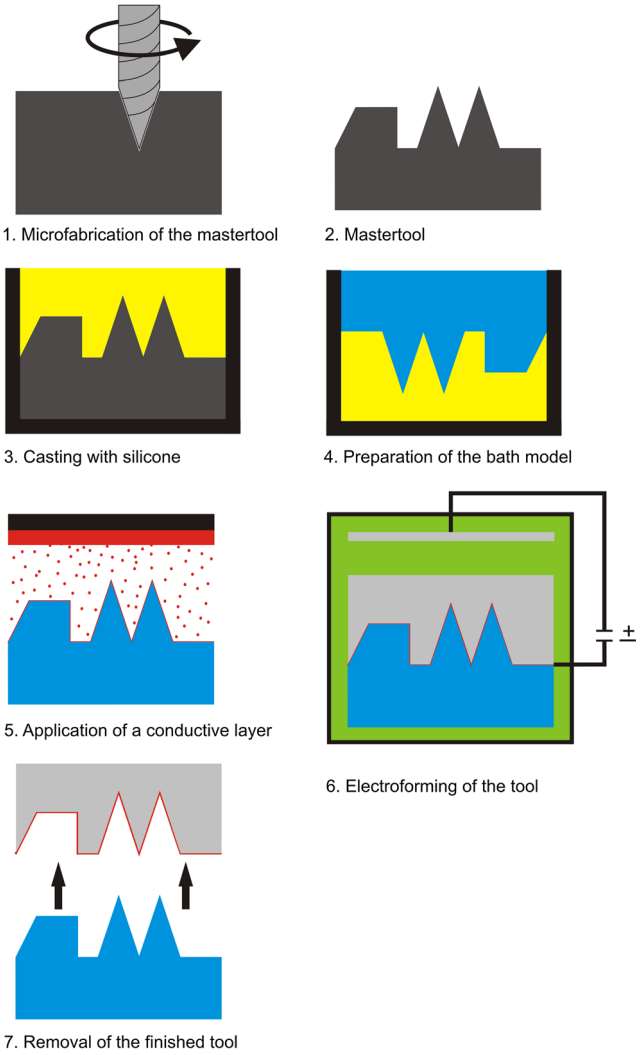

Fig. 3 Schematic view of the replication process chain

and cured for 24 h. Finally, the embedded master tool was removed from the casting box.

3.3.2 Preparation of the bath model

The silicone cast has a very high reproduction accuracy, but the mechanical properties, especially the low stiffness, are not sufficient for the electroforming process. For this reason, a bath model consisting of an epoxy resin (GH 761/D; Ebalta Kunststoff GmbH, Rothenburg ob der Tauber, Germany) was prepared (Fig. 3, step 4). The enhanced stiffness and toughness enables the deposition of nickel without deformations due to stress and strain. For this purpose, the silicone cast was coated with three layers of the epoxy resin (thickness 0.5 mm/layer). Between each layer application, a drying period of 1.5–2 h takes place. The drying period of the third layer was only 30 min to ensure a better adhesion with the following stabilizing layer. The covering layer consists of resin and embedded glass fibers (length 5–10 mm, diameter 0.5–1 mm). The whole assembly was dried for 24 h at room temperature. The silicone cast can be easily removed from the bath model.

3.3.3 Electroforming of the nickel tool

The final step of the process chain is the electroforming of the ECM tool. It was performed under constant current conditions in an aqueous nickel sulfamate electrolyte. Optimization of the bath composition and the plating conditions was described in Section 3.1. The resin is not electrically conductive at all, and, for this reason, the surface has to be covered with an appropriate metal layer. For the application of the metal layer, every method is suitable (chemical or physical vapor deposition [29, 30], sputtering techniques [31], electroless plating [32], spraying processes [33, 34]), which enables the coating with nano-sized metal layers. We used a sputtering technique [31], in which an argon plasma transfers metal atoms from a target to the bath model (Fig. 3, step 5). In principle, every metal (Cr, Ag, Ni) can be used for the sputtering process; in our case, the bath model was coated with gold. As mentioned above, the thickness of the metal layer is in the nanometer range and does not change the microstructures.

For the electroforming process (Fig. 3, step 6), the bath model was wired and put into the galvanic bath containing a commercial nickel sulfamate electrolyte (see Section 3.1.1) without any additives. The solution was stirred, filtered (pore size 4 μm), and additionally circulated using a pump. Nickel was galvanostatically deposited with a constant current density of −20 mA cm^{-2} at a pH value of 3.8 and a bath temperature

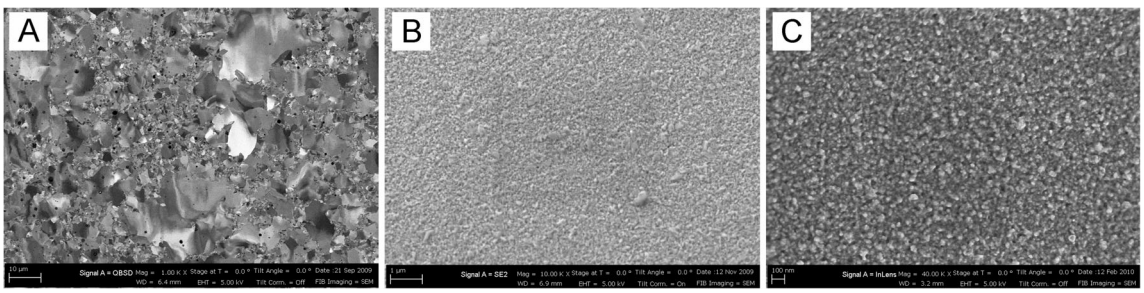

Fig. 4 SEM pictures of the nickel deposit prepared with addition of butynediol (**a**), NTA (**b**), or saccharine (**c**)

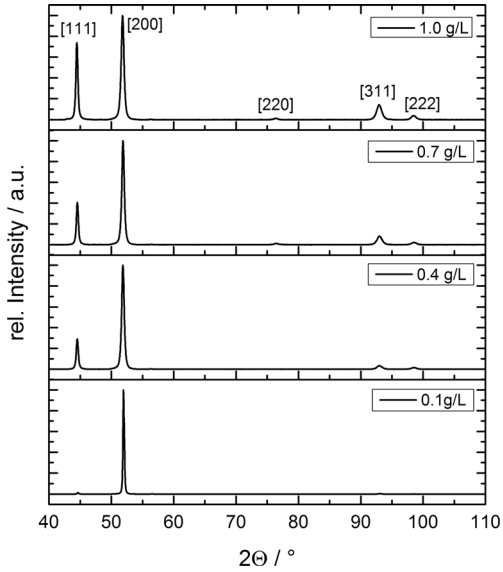

Fig. 5 Influence of the saccharine content on the preferred crystallite orientation of the deposit

of 40 °C. After 8–10 days, the tool thickness was about 2–4 mm and could be removed from the bath model.

3.4 Structural characterization of the tool

The crystallinity of the electroformed ECM tool was measured by scanning electron microscopy. A JSM-7000F (JEOL Ltd., Tokyo, Japan) microscope in bright field mode was used.

The microstructures of the edge and the back side of the ECM tool were investigated. For characterization of the crystallinity, X-ray diffraction measurements were performed. The X-ray diffraction pattern was recorded from the edge of the tool in θ–θ step mode (step size 0.02, time 6 s/step, range 35–130°) using a PANalytical X'Pert Pro diffractometer (PANalytical B.V., Almelo, the Netherlands). Secondary monochromated $CuK_{\alpha 1/2}$ radiation was used. The crystallite size, their distribution, and the microstrain content were analyzed with a self-programmed software based on a modified Warren/Averbach method [35–40]. The determination of the diffractometer resolution was done with a LaB_6 standard sample.

The three-dimensional pictures were taken with a confocal laser scanning microscope LEXT OLS 3100 (Olympus, Hamburg, Germany). Figure 10 shows the measured positions,

Table 3 Crystallite size (D_v) as function of the additive concentration

c(saccharine) (mmol L^{-1})	D_v (nm)	c(NTA) (mmol L^{-1})	D_v (nm)	c(butynediol) (mmol L^{-1})	D_v (nm)
0.49	40	0.41	48	0.23	57
1.94	31	1.66	38	0.69	55
3.40	27	2.90	24	11.63	51
4.85	26	4.14	25	16.28	53

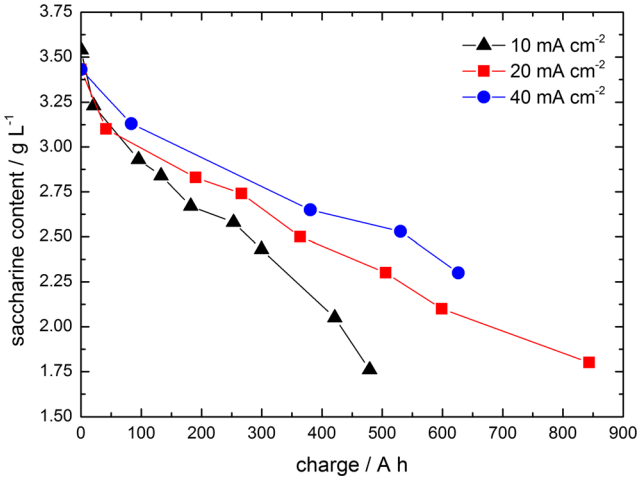

Fig. 6 Saccharine content as function of the current density for direct current plating

which represent characteristic topographies (flat areas, sharp edges, different angle geometries). For this reason, a good comparability between the workpiece and the copy is achieved. The LSM takes a series of pictures in different focal planes in a distance of about 1 µm. A mathematical algorithm transforms (OLS ver. 5.0.9; Olympus, Hamburg, Germany) the single pictures into a three-dimensional picture. The resulting *xyz* data allow the evaluation of topographical profiles as well as sectional planes. Both features were used for the qualitative and quantitative comparison between tool and copy.

4 Results and discussion

4.1 Texture, crystallite size and hardness of nickel deposits

As shown in Fig. 4, by adding saccharine, a homogeneous fine-grained microstructure consisting of crystallites with an

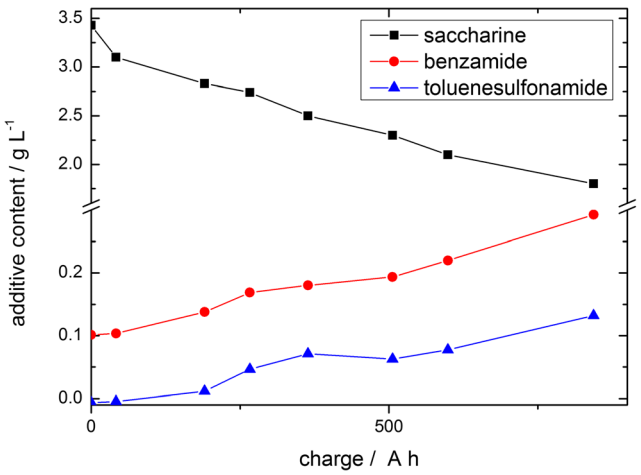

Fig. 7 Concentration profiles for saccharine and its decomposition products benzamide and toluenesulfonamide (TSA)

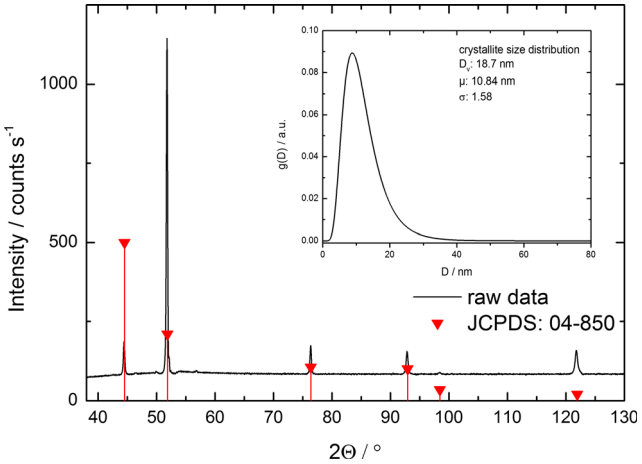

Fig. 8 X-ray diffraction pattern and corresponding crystallite size distribution of additive-free plated nickel

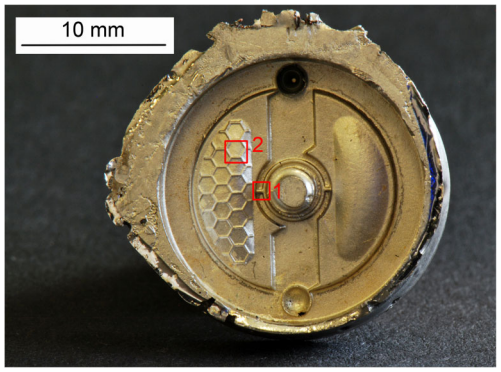

Fig. 10 Copied ECM tool. The *red squares* show the positions where the LSM pictures were taken

average crystallite size of 50 nm is produced. The addition of NTA results in a homogenization and grain refinement of the microstructure, too. Butynediol has no influence on the microstructure.

The preferred crystallite orientation was investigated using X-ray diffraction. In comparison to the crystallographic reference (PDF 04-850), the deposits from the sulfamate electrolyte show a preferred orientation in (200) direction.

Figure 5 outlines the influence of different saccharine concentrations on the preferred crystallite orientation. Increasing saccharine concentrations promote the crystallite growth in the (111) and (311) orientation. This observation can be explained by a chemical reaction of the additive (saccharine), which promotes the reduction of protons and hence the formation of $Ni(OH)_2$ in the cathodic layer. The hydroxide formation leads to the preferred growth of the (111) and (311) orientations.

The influence of NTA on the preferred crystallite orientation is similar to that of saccharine. With an increasing NTA concentration, the (200) orientation is reduced by the strong increase of a mixed (111) and (311) orientation. Using similar molar concentrations, NTA leads to a stronger pronounced (111) orientation than saccharine.

The addition of butynediol only takes effect on the preferred crystallite orientation in much higher concentrations than saccharine and NTA. Higher concentrations of butynediol promote a mixed preferred crystallite orientation in (111) and (220) direction. With increasing concentration, the (220) direction becomes more pronounced.

In order to investigate the influence of the additives on the crystallite size, the crystallite size was determined using the Warren/Averbach method [40]. The volume-weighted

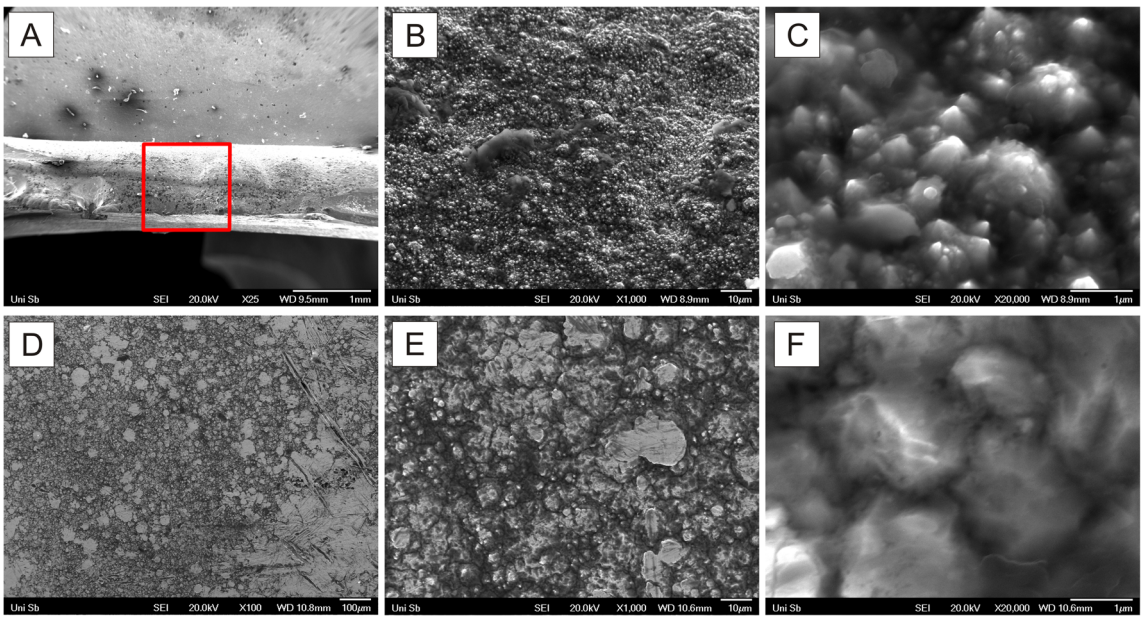

Fig. 9 SEM pictures of the replicated tool (**a**–**c** front region; **d**–**f** back side)

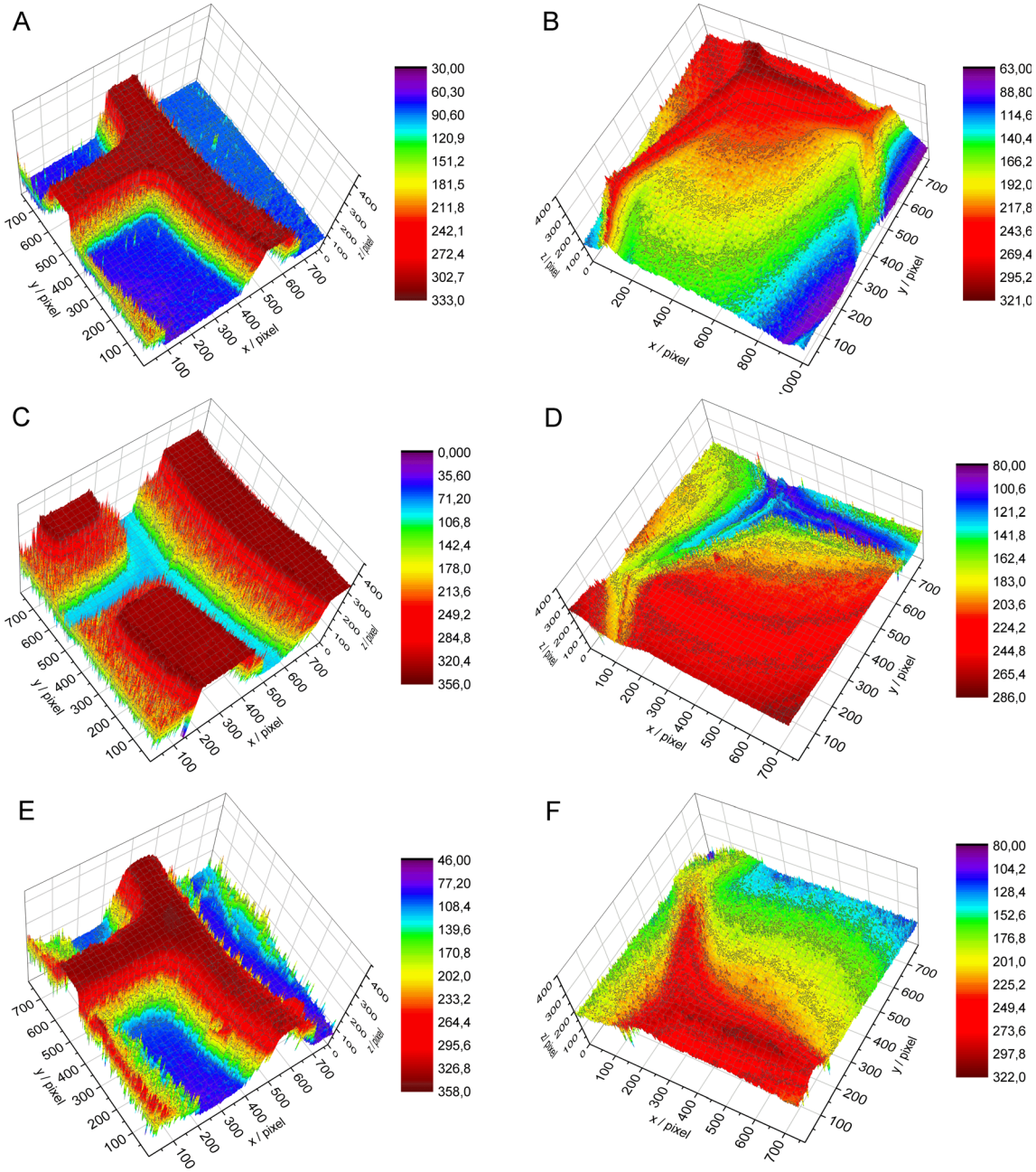

Fig. 11 Three-dimensional pictures of the characteristic positions: original tool (**a**, **b**), workpiece (**c**, **d**), copy (**e**, **f**). (**a**), (**c**), (**e**) measured at Position 1 and (**b**), (**d**), (**f**) at Position 2

crystallite sizes (D_v) as function of the molar concentration are summarized in Table 3.

The addition of 3.40 mmol L^{-1} saccharine reduces the crystallite size down to 27 nm. Higher additive concentrations have nearly no effect since the electrode surface is already covered with molecules. A further reduction of the crystallite size is in the order of the error of the used method. NTA shows a similar effect as saccharine. For butynediol, the crystallite sizes scatter around 54±3 nm. This outlines that butynediol has no significant effect on the crystallite size.

For saccharine and NTA, the Vickers hardness of the samples with the highest additive concentration was measured. The additive-free electrolyte produces deposits with a hardness of HV 249±14. For saccharine, a hardness of HV 557±5 and for NTA of HV 228±4 was measured. Although both additives cause crystallite refinement of the nickel deposits, only saccharine has a significant effect on the hardness. Saccharine doubles the hardness in comparison to the additive-free electrolyte. Because the best results in hardness were achieved by the addition of saccharine, only saccharine was used for further studies.

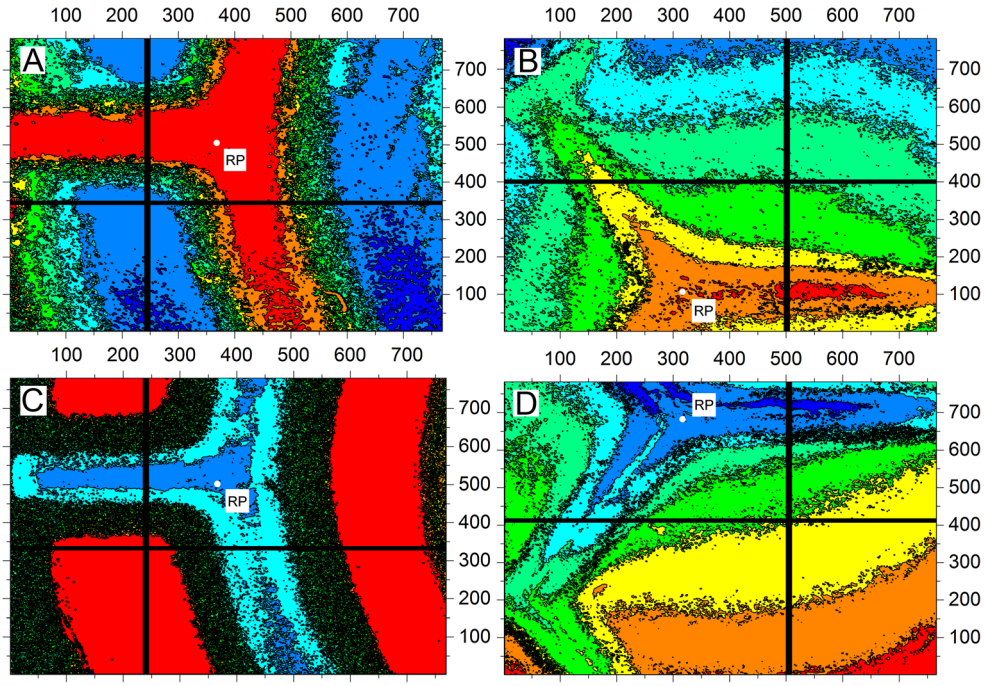

Fig. 12 Two-dimensional topographic profiles (**a**, **b** copy; **c**, **d** workpiece) with the positions of the horizontal and vertical sectional planes. *RP* indicates the reference position

4.2 Incorporation of saccharine

Since the decomposition and incorporation of saccharine occur during the deposition, it must be re-dosed. Figure 6 outlines for three different current densities the decomposition of saccharine in the electrolyte as function of the charge.

The saccharine content decreases faster for low current densities than for high current densities. In the case of low

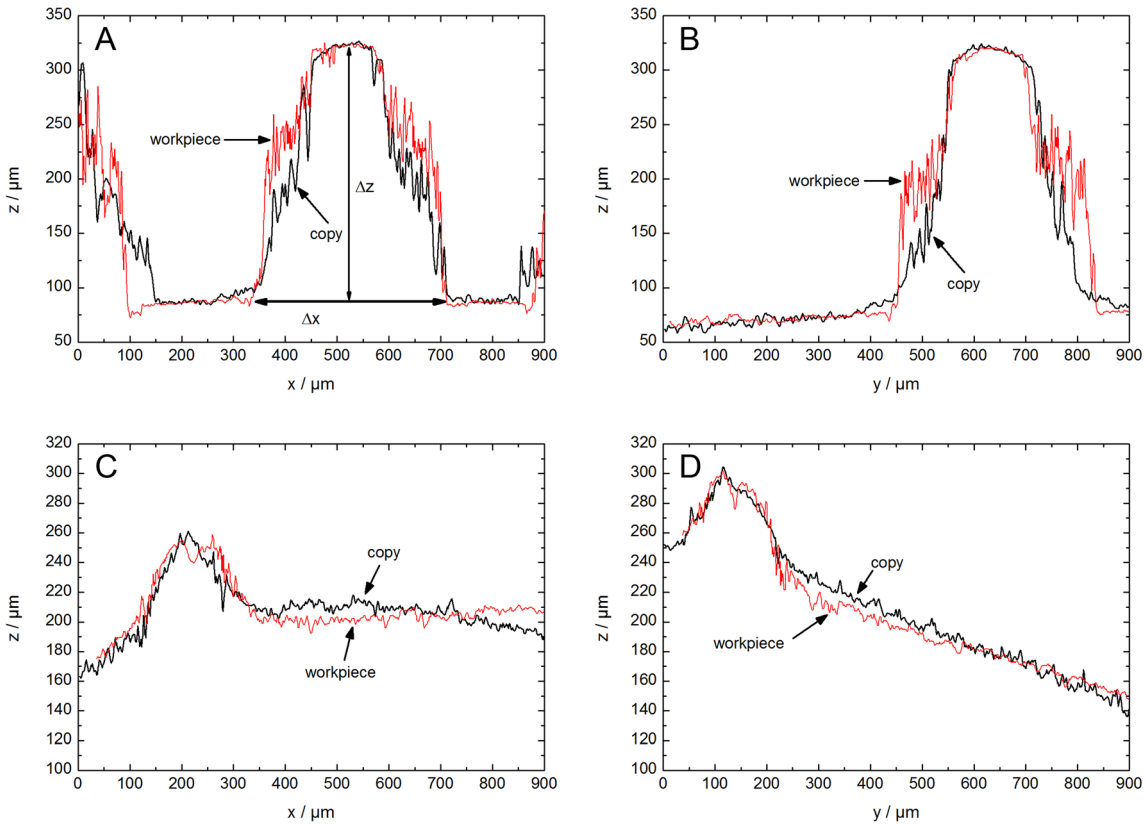

Fig. 13 Sectional planes of workpiece and copy (**a**, **b** position 1; **c**, **d** position 2)

Table 4 Dimensions of the structures and the deviations between workpiece and copy (Δx denotes the horizontal sectional plane and Δy the vertical sectional plane)

Sectional plane	Width (μm) Copy / workpiece	Height (μm) Copy / workpiece	Deviation (%) Width / height
Pos. 1, Δx	380 / 380	276 / 280	0 / 1.3
Pos. 1, Δy	415 / 398	280 / 290	4.2 / 3.4
Pos. 2, Δx	233 / 246	72 / 64	5.3 / 12.5
Pos. 2, Δy	223 / 202	72 / 70	10.4 / 2.9

current densities, a large amount of saccharine adsorbs on the cathode surface and hence a lot of saccharine will be co-deposited during the nickel deposition [41]. With high current densities, a permanent recreation of new surface can be observed and the deposition process is faster than the adsorption process. Hence, to reduce the amount of incorporated sulfur in the deposit, the current density should not be too small. The reduction in the saccharine amount during the deposition is caused by the decomposition and the occlusion. To determine the amount of incorporated sulfur, the evaluation of the decomposition products as function of the charge during the deposition was investigated. Figure 7 outlines the loss of saccharine and the increase of its decomposition products as function of the total charge.

Before starting the deposition, there are already traces of benzamide in the electrolyte. This outlines that saccharine decomposes not only due to electrochemical oxidation and reduction but also due to thermal processes and light irradiation. TSA is not present at the beginning the electrodeposition. According to the average slope of the formation of both decomposition products, their formation is much slower than the decrease of the saccharine concentration. At a current density of 20 mA cm^{-2}, the depletion rate of saccharine is about 1.8 mg $(L\ Ah)^{-1}$, whereas the total accumulation rate for the decomposition products is 0.39 mg $(L\ Ah)^{-1}$. This proves that the reduction in the saccharine concentration during the deposition is mainly affected by the occlusion of saccharine in the growing nickel deposit. For a volume of 4.5 L sulfamate electrolyte, there is an occlusion of 6.3 mg Ah^{-1} saccharine in the nickel deposit, corresponding to a sulfur content of 0.09 %.

4.3 Microstructural characterization of the nickel tool

The X-ray diffraction pattern of the additive-free plated nickel corresponds well with the standard pattern 04-850 of the JCPDS data base. The inlay of Fig. 8 shows the results of the Warren/Averbach analysis. The volume-weighted crystallite size (D_v) is 18.7 nm and the parameters of the determined lognormal distribution are μ=10.84 nm (μ divides the peak area into two equal parts) and σ=1.58 (parameter related to the width of the distribution). The data reveal that a nanostructure has been formed without the addition of organic additives. One reason for this behavior is the electrochemical deposition onto a microstructured surface. At very small edges and peaks, the electric field lines are concentrated and the local electric field at these positions is increased leading to an enhanced nuclei formation and therefore to small crystallites—without addition of any additives. A second explanation could be the secondary inhibition (see Section 2) by the formation of nickel hydroxides produced during the hydrolysis of the nickel electrolyte due to an increase of the pH value in the Helmholtz double layer. The advantage of this additive-free electrolyte is the formation of a nanostructure without the inclusion of organic additives in the metal structure of the ECM tool, and, therefore, the mechanical properties are not drastically changed during the electroforming process. The X-ray data received from the electroformed tool also show a (200) texture, which cannot be avoided without additives. Nevertheless, the mechanical stability of the tool is sufficient enough for the desired use in ECM processes.

SEM pictures of different positions are shown in Fig. 9. The microstructure of the front region (Fig. 9c) shows submicron-sized grains, which consist of agglomerated crystallites with a diameter of about 20 nm (measured by XRD). Compared to the front region, the grain size of the back is significantly increased. The grains have a diameter of about 2–4 μm. The increase of the grain size can be explained by the theory of electrocrystallization [25–27]. At the beginning of the deposition, the electric field lines at the microstructured electrode surface are very high resulting in an increased nuclei formation rate and therefore in a large amount of very small crystallites. In the advanced stage of electroforming, the surface roughness and therefore the overpotential decreases resulting in the formation of larger crystallites. The gradient in crystallite size does not influence the replication process because the smallest crystallites were formed on the structured side of the master tool.

4.4 Macrostructural characterization

In this feasibility study, the assessment of the replication accuracy was done by investigating two characteristic positions

Table 5 Calculation of the areas under the structures

Sectional plane	Area (μm^2) Copy / workpiece	Integration limits (μm) Copy / workpiece	Deviation (%)
Pos. 1, Δx	52,124 / 61,381	342–717 / 340–713	15.1
Pos. 1, Δy	53,683 / 65,316	416–836 / 438–838	17.8
Pos. 2, Δx	7069 / 7686	124–343 / 118–347	8.0
Pos. 2, Δy	6611 / 6842	20–246 / 1–180	3.4

using LSM. A photograph of the replicated tool is shown in Fig. 10. Distinctive positions are marked with red squares. Corresponding measurements were performed on the original electrode and on the workpiece shown in Fig. 2.

The recorded LSM pictures are shown in Fig. 11. In order to compare the workpiece with the copy, the digitalized (Origin 9.1; OriginLab Corp., Northampton, USA) structure profiles are transferred into two-dimensional plots, in which the sectional planes in x- and y-direction are measured. To guarantee that the positions of the sectional planes are the same for all samples, we have chosen reference points (RP) in the pictures. The reference points as well as the sectional planes are shown in Fig. 12. For the determination of the x- and y-data, an average value over 10 pixels (pixel size 1.2×1.2 µm^2) were calculated. For a better comparability, the curves of the investigated samples are overlaid (Fig. 13).

A first qualitative evaluation was done by measuring the heights (Δz) and widths (Δx and Δy) of the structures (exemplified in Fig. 13a). The results are summarized in Table 4.

It can be seen that the deviations of the copied structural characteristics (structure angles, curved areas, structure heights) vary between 0 and 12.5 %. This relatively high scattering can be explained by the used evaluation method. It is difficult to determine the exact structure boundaries, and, therefore, the measurement becomes imprecise. For this reason, another evaluation method was chosen to determine the structural accuracy of the process. The areas under the investigated structures were calculated and compared to each other (Table 5).

Compared to the evaluation above, the results show contrary deviations. The deviation values for Position 2 decrease to 8.0 and 3.4 %, respectively, whereas the deviations for Position 1 increase. In order to localize the position of the deviations in the structures, the residuals of workpiece and copy are plotted (Fig. 14).

Figure 14a and b reveals strong deviations at the vertical faces of the structure. Furthermore, a high signal noise is observed at these positions. This result can be explained by the experimental setup for the topography measurement. LSM uses a laser beam to scan the sample surface. Sample areas, which are orthogonal to the incident beam, cause less signal intensity for this position resulting in an increased signal noise. This is not the case for Position 2 consisting of low-angle faces and curved planes. In these regions, the signal-to-noise ratio is much better than for vertical flanks. This good signal-to-noise ratio at Position 2 can be found in the residual plots (Fig. 14c, d). Nevertheless, LSM is suited for the investigation of the absolute structure heights (as seen in Table 4) and the residual plots (Fig. 14a, b). More suitable methods for measuring orthogonal structures are X-ray tomography as a non-destructive method and cross-section preparation as a destructive method.

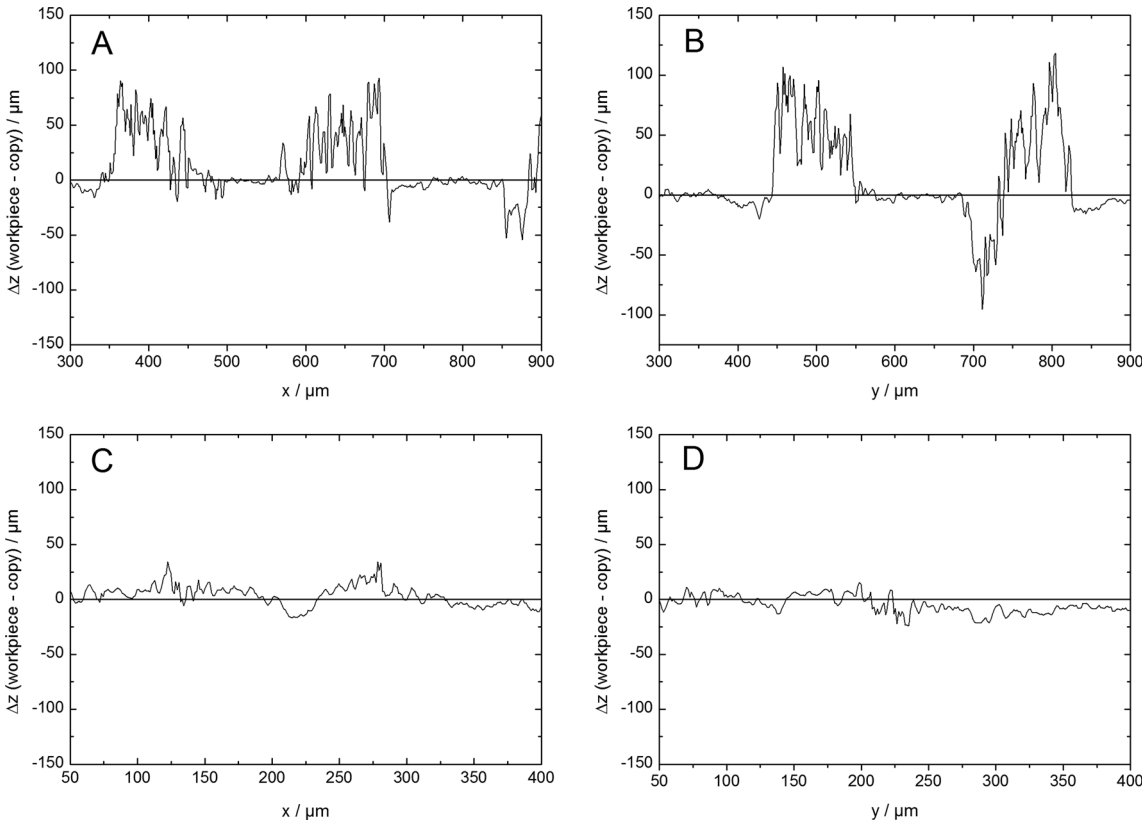

Fig. 14 Residual plots resulting from the differences between copy and workpiece (**a**, **b** Position 1; **c**, **d** Position 2)

5 Conclusions

- The surface of a PECM tool was successfully copied by using electroforming.
- LSM is a suitable method to measure the accuracy of the copy, but it depends strongly on the structural characteristic; curved and low-angle shapes as well as flat areas can be investigated precisely whereas orthogonal structures and holes cause strong signal noise, and therefore stronger deviations.
- The deviations between copy and workpiece are in the range of 3.4–8.0 % (Position 2).
- The microstructural characterization was performed by means of XRD and SEM. The X-ray diffraction pattern fits well with the JCPDS database. It shows that a nanostructure was formed with an average crystallite size of less than 20 nm. Furthermore, a texture in (200) direction is indicated. The SEM pictures show an increase of the crystallites from the structured side (about 20 nm) towards the back of the sample (2–4 μm).
- An addition of organic compounds like saccharine or NTA can improve the result of the electroforming, but the inclusion of these substances influences the properties of the deposit negatively. Thus, an additive-free electrolyte was chosen for the ECM tool replication.

Acknowledgments The project was financed by the European Union in the framework of the Interreg IVa program "Initiative Precise". The authors gratefully acknowledge Prof. Dr. Rolf Hempelmann, Prof. Dr.-Ing. Dirk Bähre, Dipl.-Ing. Sylvia Kuhn, Elfi Jungblut, Reiner Wintringer, Dipl.-Ing. Juri Kraft, and Alain Funfrock for experimental help and fruitful discussions.

References

1. Bannard J (1977) Electrochemical machining. J Appl Electrochem 7:1–29
2. McGeough JA (1974) Principles of electrochemical machining. Chapman and Hall Ltd, London
3. Datta M, Landolt D (1981) Electrochemical machining under pulsed current conditions. Electrochim Acta 26:899–907
4. Rajurkar KP, Kozak J, Wei B, McGeough JA (1993) Study of pulse electrochemical machining characteristics. CIRP Ann Manuf Technol 42:231–234
5. Bhattacharyya B, Malapati M, Munda J, Sarkar A (2007) Influence of tool vibration on machining performance in electrochemical micro-machining of copper. Int J Mach Tools Manuf 47:335–342
6. Rajurkar KP, Zhu D, McGeough JA, Kozak J, De Silva A (1999) New developments in electro-chemical machining. Ann CIRP 48(2):567–579
7. Weinmann M, Stolpe M, Busch R, Natter H (2015) Eletrochemical dissolution behaviour of Ti90Al6V4 and Ti60Al40 used for ECM applications. J Solid State Electrochem 19(2):485–495
8. Kozak J, Rajurkar KP, Makkar Y (2004) Selected problems of micro-electrochemical machining. J Mater Process Technol 149: 426–431
9. Schuster R, Kirchner V, Allongue P, Ertl G (2000) Electrochemical micromachining. Science 289:98–101
10. Bhattacharyya B, Munda J, Malapati M (2004) Advancement in electrochemical micro-machining. Int J Mach Tools Manuf 44: 1577–1589
11. Li XH, Wang ZL, Zhao WS, Hu FQ (2007) Pulsed micro-electrochemical machining technology. Key Eng Mater 339:327–331
12. Zhang Z, Wang Y, Chen F, Mao W (2011) A micro-machining system based on electrochemical dissolution of material. Russ J Electrochem 47:819–824
13. Leo Kumar SP, Jerald J, Kumanan S, Prabakaran R (2014) A review on current research aspects in tool-based micromachining processes. Mater Manuf Process 29:1291–1337
14. Fu WK, He N, Li L, Zhao M, Bian R (2014) Research on micromechanical drilling of micro-hole array in PVC mask. Mater Sci Forum 770:239–243
15. Asad ABMA, Masaki T, Rahman M, Lim HS, Wong YS (2007) Tool-based micro-machining. J Mater Process Technol 192–193: 204–211
16. Rahman M, Asad ABMA, Wong YS (2014) Introduction to advanced machining technologies. Compr Mat Process 11:1–13
17. Tangwarodomnukun V, Likhitangsuwat P, Tevinpibanphan O, Dumkum C (2015) Laser ablation of titanium alloy under a thin and flowing water layer. Int J Mach Tools Manuf 89:14–28
18. Weinmann M, Weber O, Bähre D, Munief W, Saumer M, Natter H (2014) Photolithography-electroforming-pulse electrochemical machining: an innovative process chain for the high precision and reproducible manufacturing of complex microstructures. Int J Electrochem Sci 9:3917–3927
19. Natter H, Hempelmann R (2008) Nanocrystalline metals prepared by electrodeposition. Z Phys Chem 222:319–354
20. Natter H, Hempelmann R (2003) Tailor-made nanomaterials designed by electrochemical methods. Electrochim Acta 49:51–61
21. Fischer H (1973) Aspects of inhibition in electrodeposition of compact metals II. Effects of morphological interface inhibition. Electrodeposition Surf Treat 1(4):319–337
22. Hamann CH, Vielstich W (2005) Elektrochemie. Wiley-VCH, Weinheim
23. Puippe JC, Leaman F (1986) Theory and practice of pulse-plating. ASEF, Orlando
24. Vetter KJ, Bachmann KJ (1967) Zur Kristallisationsüberspannung. Z Phys Chem 53:9–28
25. Amblard J, Epelboin I, Froment M, Maurin G (1979) Inhibition and nickel electrocrystallization. J Appl Electrochem 9:233–242
26. Amblard J, Froment M, Maurin G, Mercier D, Trevisan-Pikacz E (1982) The electrocrystallization of nickel on vitreous carbon a kinetic and structural study of nucleation and coalescence. J Electroanal Chem Interfacial Electrochem 134(2):345–352
27. Amblard J, Froment M, Maurin G, Spyrellis N, Trevisan-Souteyrand E (1983) Nickel electrocrystallization—from nucleation to textures. Electrochim Acta 28:909–915
28. Amblard J, Froment M, Spyrellis N (1977) Origine des textures dans les depots electrolytiques de nickel. Surf Technol 5(3):205–234
29. Sathiyanarayanan S, Rajagopal G, Palaniswamy N, Raghavan M (2005) Corrosion protection by chemical vapor deposition: a review. Corros Rev 23(4–6):355–370
30. Helmersson U, Lattemann M, Bohlmark J, Ehiasarian AP, Gudmundsson JT (2006) Ionized physical vapor deposition (IPVD): a review of technology and applications. Thin Solid Films 513:1–24
31. Seah MP, Nunney TS (2010) Sputtering yields of compounds using argon ions. J Phys D Appl Phys 43:1–13
32. Larson C, Smith JR (2011) Recent trends in metal alloy electrolytic and electroless plating research: a review. T I Met Finish 6:333–341

33. Blink J, Farmer J, Choi J, Saw C (2009) Applications in the nuclear industry for thermal spray amorphous metal and ceramic coatings. Metall Mater Trans 40A:1344–1354
34. Moridi A, Hassani-Gangaraj SM, Guagliano M, Dao M (2014) Cold spray coating: review of material systems and future perspectives. Surf Eng 30(6):369–395
35. Natter H, Hempelmann R (1996) Nanocrystalline copper by pulsed electrodeposition: the effects of organic additives, bath temperature, and pH. J Phys Chem 100:19525–19532
36. Natter H, Schmelzer M, Löffler MS, Krill CE, Fitch A, Hempelmann R (2000) Grain-growth kinetics of nanocrystalline iron studied in situ by synchrotron real-time x-ray diffraction. J Phys Chem B 104:2467–2476
37. Warren BE, Averbach LE (1950) The effect of cold-work distortion on x-ray patterns. J Appl Phys 21:595–599
38. Warren BE, Averbach LE (1952) The separation of cold-work distortion and particle size broadening in x-ray patterns. J Appl Phys 23:497
39. Warren BE (1990) X-ray diffraction. Dover Publications, INC, New York
40. Krill CE III, Helfen L, Michels D, Natter H, Fitch A, Masson O, Birringer R (2001) Size-dependent grain-growth kinetics observed in nanocrystalline Fe. Phys Rev Lett 86(5):842–845
41. Dini JW (1993) Electrodeposition: the materials science of coatings and substrates. Noyes, Park Ridge